PHYSICS

High-speed thin-film lithium niobate quantum processor driven by a solid-state quantum emitter

Patrik I. Sund[1]†, Emma Lomonte[2,3,4]†, Stefano Paesani[1]*, Ying Wang[1], Jacques Carolan[1,5], Nikolai Bart[6], Andreas D. Wieck[6], Arne Ludwig[6], Leonardo Midolo[1], Wolfram H. P. Pernice[2,3,4,7], Peter Lodahl[1], Francesco Lenzini[2,3,4]*

Scalable photonic quantum computing architectures pose stringent requirements on photonic processing devices. The needs for low-loss high-speed reconfigurable circuits and near-deterministic resource state generators are some of the most challenging requirements. Here, we develop an integrated photonic platform based on thin-film lithium niobate and interface it with deterministic solid-state single-photon sources based on quantum dots in nanophotonic waveguides. The generated photons are processed with low-loss circuits programmable at speeds of several gigahertz. We realize a variety of key photonic quantum information processing functionalities with the high-speed circuits, including on-chip quantum interference, photon demultiplexing, and reprogrammability of a four-mode universal photonic circuit. These results show a promising path forward for scalable photonic quantum technologies by merging integrated photonics with solid-state deterministic photon sources in a heterogeneous approach to scaling up.

INTRODUCTION

Sustained progress of quantum technologies has enabled quantum hardware to compete with and surpass the capabilities of classical supercomputers (1–4). However, challenges remain to reach controllable quantum systems at scale, as required for currently known practical applications and fault-tolerant quantum technologies (5). Photonics is a promising platform for unlocking scalable quantum hardware (6, 7), with the capacity to enable long-range quantum networks (8, 9), interconnections between multiple quantum devices (10), and large-scale photonic circuits for quantum computing and simulation (11–14). Central to photonic quantum technologies is the generation of high-quality photonic states and fast low-loss programmable circuits for their routing and processing (15, 16). In recent years, progress has been achieved in developing near-ideal high-efficiency sources of indistinguishable photons, with solid-state quantum emitters, such as quantum dots (QDs), standing out as excellent candidates for the realization of on-demand single-photon sources (SPSs) (17–20). Low-loss optical circuits that can be rapidly reprogrammed (typically gigahertz rates required) are central for key tasks in photonic quantum information processing, such as multiplexing or demultiplexing of SPSs (21–23), routing for fusion networks, and feedforward operations for fusion-based quantum computation (15, 24). However, a platform satisfying all requirements for the integration of gigahertz speed low-loss circuits at scale has so far been

elusive. Standard approaches, such as thermal modulators or micro-electromechanical systems (MEMS) in the SOI or SiN platforms, are limited to operating speeds up to megahertz (14, 25, 26), while high-speed free-carrier modulators add substantial phase-dependent photon loss (27). Very recently, programmable integrated circuits based on piezo-optomechanical actuators coupled to SiN waveguides with a modulation speed up to approximately 120 MHz were demonstrated at both room and cryogenic temperatures (28). Still, the scalability of these devices is currently limited by high insertion loss (>3 dB) and a low modulation efficiency (voltage-length product $\simeq$50 V · cm).

In this context, single-crystal thin lithium niobate [LiNbO$_3$ (LN)] films bonded on a silica insulating substrate [lithium niobate on insulator (LNOI)] have emerged in recent years as a particularly promising platform. Because of their strong electro-optical properties, high transparency, and high index contrast, integrated circuits with compact footprints and low propagation loss can be implemented with tunable phase shifters having a modulation bandwidth above several gigahertz (29–31).

The wide transparency range of LN makes these circuits also especially attractive for operation with a variety of solid-state quantum emitters, which are characterized by an emission spectrum typically at visible or near-infrared wavelengths (32, 33). Moreover, electro-optic modulators (EOMs) implemented in LN are compatible with operation at cryogenic temperature (34–36), making full-system integration with QDs and high-quality superconducting nanowire single-photon detectors (SNSPDs) an additional promising prospect (36–38). However, programmable multimode LNOI circuits for quantum information processing at the single photon regime have yet to be demonstrated. Here, we report on the experimental realization of a reconfigurable LNOI quantum photonic processor for the control and operation of quantum states of light emitted from a QD SPS. The device is designed to feature low propagation loss, efficient coupling to a QD photon emitter via a fiber-to-chip interface in the targeted 900- to 950-nm wavelength range [typical emission wavelength of indium gallium arsenide (InGaAs) QDs],

[1]Center for Hybrid Quantum Networks (Hy-Q), Niels Bohr Institute, University of Copenhagen, Blegdamsvej 17, Copenhagen DK-2100, Denmark. [2]Institute of Physics, University of Muenster, Muenster 48149, Germany. [3]CeNTech—Center for Nanotechnology, Muenster 48149, Germany. [4]SoN—Center for Soft Nanoscience, Muenster 48149, Germany. [5]Wolfson Institute for Biomedical Research, University College London, London, UK. [6]Lehrstuhl für Angewandte Festkörperphysik, Ruhr-Universität Bochum, Universitätsstrasse 150, Bochum D-44780, Germany. [7]Heidelberg University, Im Neuenheimer Feld 227, Heidelberg 69120, Germany.
*Corresponding author. Email: stefano.paesani@nbi.ku.dk (S.P.); lenzini@uni-muenster.de (F.L.)
†These authors contributed equally to this work.

and modulators that enable programming the quantum processor up to gigahertz speed. By injecting single photons emitted by a waveguide-integrated QD source into the LNOI optical circuitry, we show prototypical key functionalities needed for photonic quantum information processing, including multiphoton interference, active four–spatial mode routing and demultiplexing of a temporal stream of photons, and the operation of a 4 × 4 reconfigurable universal unitary circuit (*39*).

RESULTS

Integrated photonic platform

In Fig. 1A, we report a schematic of the geometry used for the realization of single-mode (SM) LNOI waveguides. Optical circuits are implemented as rib waveguides with a 180-nm etching depth, fabricated by electron-beam lithography (EBL) and argon etching on a 300-nm-thick X-cut LN film bonded on a silica-on-silicon substrate (see Materials and Methods for more details). After etching, the waveguides are clad with a ≃550-nm-thick electrically cured hydrogen silsesquioxane (HSQ) layer. The angle of the waveguide sidewalls (measured with an atomic force microscope) is ≃60°, and the top waveguide width of 550 nm ensures SM operation around 940-nm wavelength, the typical emission wavelength for InGaAs QDs used in this work, for transverse electric–polarized light.

The fabrication of photonic integrated circuits (PICs) operating at the short emission wavelength of InGaAs QDs comes with the disadvantage of increased propagation loss due to sidewall scattering, whose magnitude scales inversely with the third power of the operation wavelength (*40*), when compared with the values attainable for telecom LNOI waveguides. For this reason, we chose to use SM waveguides only for the realization of bends and directional couplers—where it is more likely to excite higher-order modes—and to adiabatically enlarge the waveguide width up to 1 μm in the straight sections of the optical circuitry to reduce the overlap between the TE optical mode and the waveguide sidewalls (see Fig. 1B). Using this approach, we were able to measure a low propagation loss coefficient down to 0.84 dB/cm at λ = 940 nm (see the Supplementary Materials for more details).

The LNOI PIC is optically coupled to SM fibers using apodized grating couplers with a negative diffraction angle, designed by following the approach of (*41*). The best coupling efficiency of our gratings was measured around 930-nm wavelength and found to be −3.4 dB (see Fig. 1C and Materials and Methods for further details). This measured value compares well with the best ones obtained at telecom wavelength for gratings etched on a pure LNOI platform, i.e., without any use of a back reflector for improving the grating directivity or additional material layers for increasing the grating strength [see, e.g., (*42*) for a review on recent progress]. We numerically estimate that with the aid of a metal back reflector underneath the buried oxide layer, our couplers can achieve an insertion loss of <1 dB. The LNOI PICs demonstrated here can therefore offer an efficient approach for interfacing fast optical switches and circuits to optical fibers.

For the realization of electro-optically tunable waveguide circuits, we use as a main building block Mach-Zehnder interferometers (MZIs) consisting of two 50:50 directional couplers and an electrically tunable phase shifter (see Fig. 1D). The phase shifter is implemented by patterning three 1.25-mm-long gold electrodes in a ground-signal-ground configuration along the *y* axis of the crystal to provide an efficient overlap between the fundamental TE mode of the waveguide and the *z* component of the applied
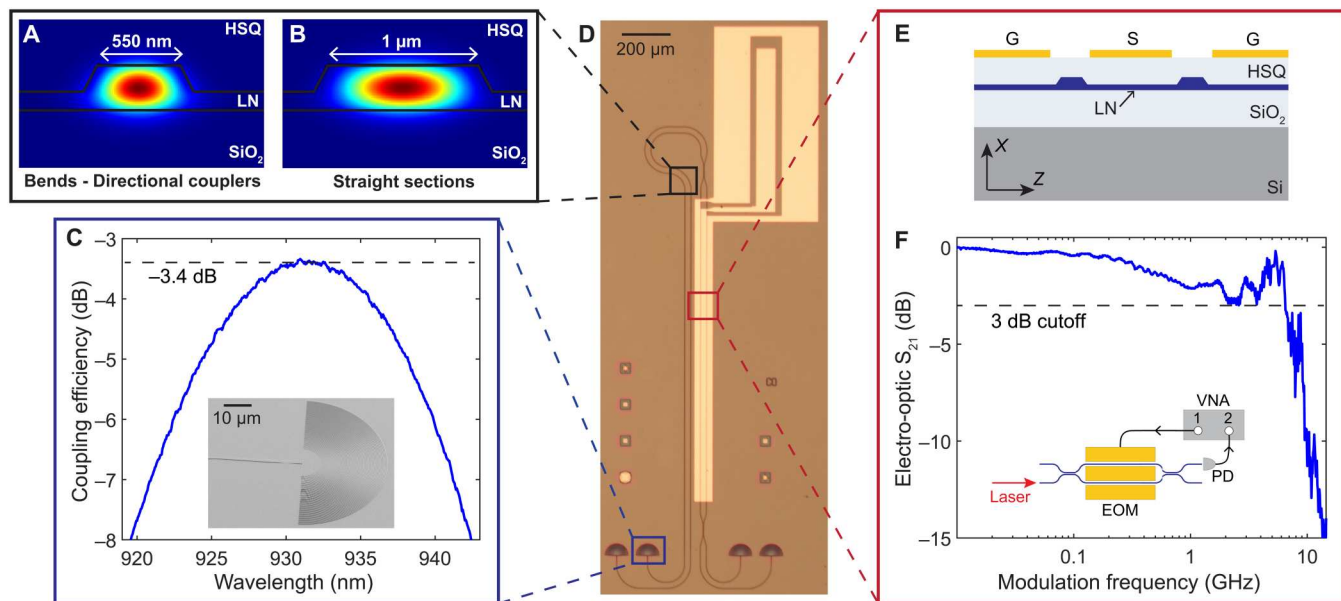
Fig. 1. Overview of the platform. (**A** and **B**) Schematics of the designed waveguide geometry, tailored for the quantum emitter λ ≃ 940 nm operation wavelengths, for (A) SM waveguides used in bends and directional couplers, and (B) multimode straight waveguides. Color-coded is the field intensity of the fundamental TE waveguide mode. (**C**) Measured coupling efficiency of the fabricated grating couplers as a function of the input laser wavelength, with a peak efficiency of −3.4 dB. The inset shows a scanning electron micrograph image of the coupler. (**D**) Optical microscope image of an electrically tunable MZI. (**E**) Schematic of the cross section of the electro-optic phase shifter. (**F**) Modulation bandwidth of the MZI measured with a VNA. The data show a 3-dB cutoff at approximately 6.5 GHz. Inset, schematic of the setup used in the measurement.

electric field via the highest electro-optic component ($r_{33} \simeq 30$ pm/V) of the LN susceptibility tensor. Unlike more common implementations of EOMs in LNOI, where signal and ground electrodes sit at the two sides of the waveguide (30, 31), here, we opted to pattern them atop the HSQ cladding (see Fig. 1E). This choice is made to enable a nearly lossless crossing of the electrodes with the waveguides without any need for additional fabrication steps. The fabricated modulators displayed a half-wave voltage (V_π) of approximately 4.5 V, corresponding to a small voltage-length product $V_\pi L \simeq 0.6$ V · cm, and a high extinction ratio $\simeq 21$ dB. The insertion loss of a single MZI, which includes two directional couplers, propagation loss in the waveguides, and metal-induced absorption loss due to the presence of the electrodes, was estimated equal to $\simeq 0.8$ dB (see Materials and Methods).

To test the high-speed performance of the modulators, we make use of the setup schematically depicted in the inset of Fig. 1E. The phase shifter is driven with a small-amplitude radio frequency signal from port 1 of a vector network analyzer (VNA), while port 2 is connected to a fast photodiode (Newport, 1544 B) optically coupled to one of the two outputs of the MZI. The resulting S_{21} parameter—defined as the ratio between the power measured at port 2 and the power leaving from port 1—is plotted in Fig. 1F normalized to its maximum value, and provides a direct estimation of the MZI electro-optic bandwidth. From the data, we record a 3-dB cutoff frequency of the modulator at approximately 6.5 Ghz, demonstrating the high-speed capabilities of the fabricated PICs.

On-chip quantum interference

A central figure of merit in photonic quantum information processing is the visibility of multiphoton quantum interference, typically quantified as the two-photon interference visibility in Hong-Ou-Mandel (HOM) experiments. Incorporating simultaneously the detrimental effects of imperfect photonic circuitry, source distinguishability, and purity, this quantity is essential in determining the dominant stochastic noise in photonic quantum computing schemes (16) and the computational complexity limits in photonic sampling algorithms (43). We thus start by performing on-chip HOM experiments to test the performance of our platform for photonic quantum information processing with the experimental scheme depicted in Fig. 2A.

For single-photon generation, we use a self-assembled indium arsenide (InAs) QD embedded in a GaAs photonic and electronic nanostructure in a 1.6-K cryostat. The device comprises a single-sided photonic crystal waveguide and a shallow-etched waveguide grating for efficient photon generation, and a hetero-diode to suppress electrical noise and Stark-tune the emission wavelength (19). See Materials and Methods for more details. We create a two-photon input state from a stream of single photons emitted by the QD using an off-chip demultiplexer to split up pairs of consecutive photons into two distinct paths, one of which is delayed such that the photons arrive at the chip simultaneously. The photons are sent into an integrated MZI containing a tunable electro-optic phase shifter. The electrodes constituting the phase shifter are connected to an electronic probe, allowing for control of the internal phase in the MZI. Photons are then routed off-chip to SNSPDs for coincidence detection. On-chip HOM interference is studied by applying a varying phase to the high-speed modulator of the MZI interferometer and measuring the fringe of the coincidence counts at the output (44–46). The measured HOM fringe visibility of 92.7 ±

0.7% (see Fig. 2B) is consistent with the corresponding HOM visibility measured off-chip (see Materials and Methods). This testifies that the fabricated PIC does not add stochastic noise on the processed photonic states [e.g., due to imperfect phase shifting or beam splitting, temporal mismatches, excitation of higher-order modes in the waveguides, or TE–transverse magnetic (TM) intermodal conversion (47)], certifying the high quality of the developed circuits as quantum photonic processing units.

Integrated single-photon router

Fast photon routers play an important role in photonic quantum computing schemes. For example, routers can be used in conjunction with measurement and feed forward to construct multiplexing schemes, turning inherently probabilistic quantum photonic processes into near-deterministic operations (48–50). Alternatively, taking advantage of the capability of deterministic quantum emitters, streams of emitted photons can be routed into multiple spatial outputs to enable networking schemes that reduce resource overheads in photonic quantum computing architectures (15), as well as demultiplexing schemes that turn a single deterministic SPS into multiple sources (51).

Making use of the capability to integrate fast phase shifters on the LNOI platform compatible with the quantum emitter wavelengths, we demonstrate a fully on-chip photon router for the QD-emitted photons. In particular, starting from a stream of single photons emitted from the QD at a fixed rate, we implement a 1 × 4 demultiplexer. The demultiplexer consists of three fast electro-optic MZI switches, which are cascaded in a tree-shaped network, as schematized in Fig. 3B (see Fig. 3A for a device microscope image). It processes sequences of four single photons emitted by the QD with a temporal separation of 13.8 ns, switching each photon deterministically into its own dedicated spatial mode. Figure 3C shows time traces for four output detectors with respect to the pulse sequence. The average probability of switching a photon in the four-photon sequence to its dedicated mode is measured to be 96.2%, corresponding to an average suppression of −14.2 dB for unwanted photons. Such success probability is conditional upon photon detection (i.e., does not include loss) and shows the performance of rapidly programming the device to implement the desired time-dependent routing transformation. This directly illustrates the highly promising potential of the LNOI platform for photon routing of deterministic resource states produced by QDs.

Universal four-mode interferometer

Programmable multimode quantum photonic interferometers are central in the implementation of core functionalities in photonic quantum technologies, e.g., multiphoton gates and fusion measurements (24, 52), and to realize circuits for quantum computational advantage experiments or analog quantum simulation (3, 4, 53, 54). To showcase the capabilities of the QD-LNOI platform for this class of tasks, we implement a universal 4 × 4 interferometer constructed from a network of 6 MZI and 10 phase modulators, as shown in Fig. 3E. The interferometer implements a scheme from Clements et al. (39), whereby the unitary transformation enacted by the interferometer is controlled by the phases applied to the modulators, allowing for the device to implement any arbitrary linear-optical unitary transformation on the four input waveguides. We show that the interferometer can be programmed from implementing a
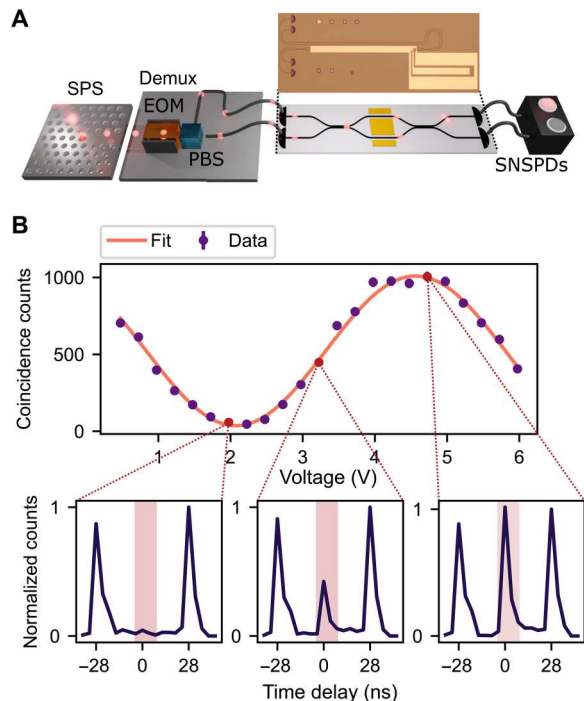
Fig. 2. Measurement of on-chip quantum interference. (A) Schematic of the experimental setup. Photons generated by a QD SPS are sent into a two-mode demultiplexer consisting of a resonantly enhanced EOM and a polarizing beam splitter (PBS). The photons are subsequently collected into fibers and injected into the LNOI chip by a fiber array. Controlling the delay on one of the demultiplexer arms ensures that the photon pairs arrive at the device simultaneously, and fiber polarization controllers are used to optimize coupling into the TE mode. The output photons are collected via the same fiber array and routed to SNSPDs for coincidence detection. Inset: Image of the MZI device used. **(B)** Recorded coincidence data at zero time delay (shaded red areas in the insets) for varying applied voltages. Minima and maxima in the observed HOM fringe correspond to applied phases of $\phi_{min} = \pi/2 + k\pi$ and $\phi_{max} = k\pi$, respectively, with k an integer number. The error bars are estimated from Poissonian statistics and are smaller than the data points. The HOM visibility of the quantum interference is determined from a curve fit (orange line) to be 92.7 ± 0.7%. Insets: Coincidence histograms for three different applied voltages.

structured matrix (an approximate permutation matrix resulting from applying no voltage to the modulators) to implementing a randomized matrix obtained by driving all the phase shifters simultaneously (see the Supplementary Materials). In Fig. 3 (F and G), we report the measured input-output probability distributions for the two cases, obtained by photon coincidence detection for all possible collision-free two-photon configurations, i.e., combinations with no more than one photon per mode. The different input states were prepared by demultiplexing a stream of photons from the QD off-chip into two separate fibers and routing these two fibers to all possible collision-free two-photon input configurations (see Fig. 3E). The measured distributions are compared with theoretical predictions obtained by reconstructing the unitary matrices from the experimental data (see the Supplementary Materials for more details). We find a mean statistical fidelity to the implemented transformation of 96.3% for the approximate permutation matrix and of 95.5% for the randomized matrix.

DISCUSSION

The demonstrated exemplary circuits show the promise of the developed LNOI platform for processing photons from emerging solid-state deterministic sources. To fully enable scalable quantum technologies, further optimization of the platform is, however, required. To improve the transmission loss at these wavelengths, besides improving our current fabrication process to reduce roughness, the use of a thinner LN film would enable the realization of SM waveguides with a larger width and to mitigate the effect of sidewall scattering. The use of a cladding with a higher refractive index than HSQ (e.g., silicon oxynitride) can also be beneficial at the expense of a larger waveguide footprint due to the lower index contrast. A large improvement in the efficiency of the grating couplers can be achieved by patterning a metal back reflector underneath the buried oxide layer. This can, for example, be accomplished via back-side etching of the silicon handle, with a fabrication process analogous to the one preliminary demonstrated in (55).

System integration of all the used quantum devices on LNOI—sources, circuits, and detectors—provides an additional promising direction for lowering the overall system loss. In this direction, direct integration of SNSPDs together with a reconfigurable LNOI component has been recently experimentally demonstrated using the same material stack used in this work (36). Heterogeneous integration of quantum emitters directly onto the LNOI waveguides could be realized with a pick-and-place technique that has recently emerged as a highly promising approach (37). Alternatively, photonic wire bonds fabricated by two-photon absorption lithography might be used for interfacing optical circuits implemented in heterogeneous photonic platforms (56).

In conclusion, high-speed LNOI quantum processors provide a route to scale up quantum photonic technologies by leveraging the mature and advanced on-demand sources realized with solid-state quantum emitters in photonic nanostructures. Moving forward, further optimization of the platform is required to reduce coupling and propagation loss, which will be realized in a close interplay between device design and PIC fabrication optimization. Fault-tolerant quantum computing architectures demand typical loss levels of ≲10% per photon (24, 57), which appears feasible with the technology after full-circle optimization of source, processor, and detector, and will be an exciting future research and engineering challenge. With such an approach, only a few tens of interconnections between individual quantum emitters and gigahertz-speed reconfigurable devices suffice for fault-tolerant photonic quantum computing at scale (15).

MATERIALS AND METHODS
Fabrication of the LNOI PICs

The LNOI PICs are fabricated on a 300-nm-thick X-cut LN film bonded on a silica-on-silicon wafer, with a Si thickness of 500 m and a SiO₂ thickness of 4.7 m (wafer produced by NanoLN). As a first step, gold markers for EBL alignment are patterned on the plain LN film with a standard lift-off process. Photonic circuits are afterward patterned by EBL with a negative resist (AR-N 7520.18), followed by Ar etching with an inductively coupled plasma system. After etching and resist stripping, an RCA-1 cleaning process is used to remove the redeposition of sputtered material on the waveguide sidewalls caused by the physical Ar etching. Next, the
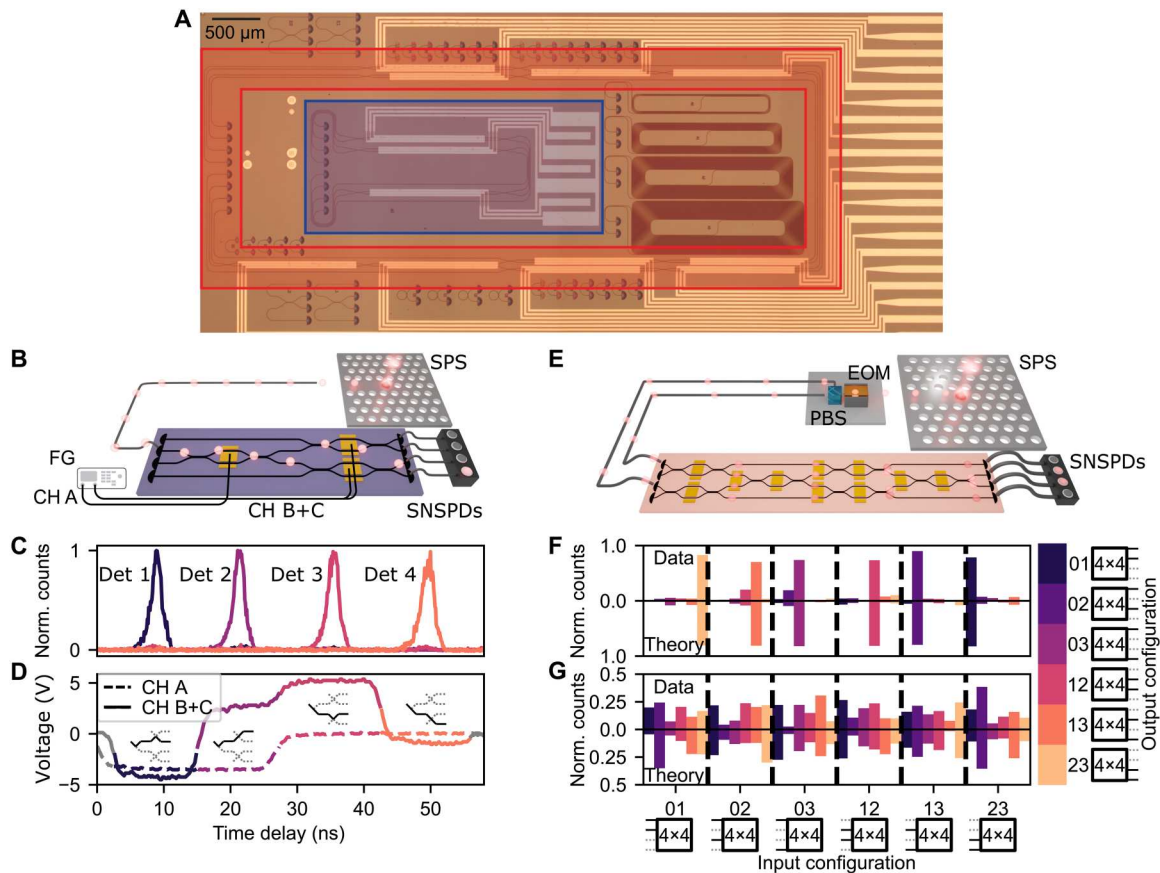
Fig. 3. Photon processing in multimode high-speed integrated circuits. (**A**) Optical image of the chip. The photon router structure is highlighted in blue, and the 4 × 4 universal interferometer is highlighted in orange. (**B**) Schematic of the experimental setup used to perform active 1 × 4 demultiplexing of a stream of single photons produced by the QD. Photons are directly coupled in and out of the chip using a fiber array, and their time of arrival is recorded via SNSPDs and a time tagger. Fast electrical control is performed via a function generator (FG) connected to the modulators via a probe station, where a channel is used to individually address the MZI in the first layer and the other channel is split to drive both MZIs in the second layer in parallel. (**C**) Normalized photon counts in the four output waveguides within the time interval of a four-photon sequence. (**D**) Associated pulse sequences, with corresponding switching network configurations shown as insets. (**E**) Schematic of the experimental setup for the universal 4 × 4 interferometer. The optical part is equivalent to that described in Fig. 2. The 10 high-speed modulators used are electrically connected via a probe station and driven by a multichannel function generator. (**F** and **G**) Experimental data (top) and estimated theoretical (bottom) collision-free input-output probability distributions when programming the interferometer to implement an approximate permutation matrix (F) and a randomized unitary matrix (G), with estimated statistical fidelities of 96.3 and 95.5%, respectively. The horizontal index indicates the input configuration in terms of the mode indices of the first and second photon, and the color corresponds to the output configuration. Dashed lines separate different input configurations.

waveguides are clad with a ≃550-nm-thick electrically cured HSQ layer and annealed at 400°C for 1 hour to reduce the absorption loss of the LN crystal. As a last step, the modulators are patterned atop the HSQ cladding with a standard lift-off process.

Solid-state quantum emitter details

Self-assembled InAs QDs are adopted to generate single photons. A GaAs pin diode structure was fabricated on a sacrificial $Al_{.75}Ga_{.25}As$ layer, resulting in a 180-nm-thick membrane. QDs were introduced in the middle of the membrane. Photonic and electronic nanostructures to interface with the QDs are fabricated via mature fabrication techniques developed for this solid-state platform ([7]). First, high-quality metal gates are fabricated and used to suppress electronic noise, as well as for tuning the QDs' emission wavelength via Stark shift ([19], [58]). To improve the single-photon collection efficiency, single-sided photonic crystal waveguides were used ([59]), which were terminated with a row of mirroring holes reflecting

the single photons emitted on the reflection side of the waveguide. On the other side of the waveguide, a shallow-etched grating coupler is used for off-chip coupling, with a distributed Bragg reflector grown below the sacrificial layer that efficiently shapes the mode for coupling to an SM fiber. With this source, we generate 15.6 million photons/s in a fiber for a QD source pumped at a repetition rate at 72.6 MHz ([59]), where residual photon losses are dominated by optical elements in the collection path and can be readily improved even further. The sample was placed in a 1.6-K cryostat, and pulsed resonant excitation was used to achieve high-quality single-photon generation. The source was characterized with a standard free-space single-photon spectroscopy setup to achieve a near-unity single-photon purity of $g^{(2)}(0) = 0.005 \pm 0.001$, i.e., 99.5% single-photon purity, and a degree of indistinguishability of 94.5 ± 1.7% between subsequently emitted photons in a HOM interference experiment.

Measurement of the grating coupler efficiency

The efficiency per coupler reported in Fig. 1C is estimated as the square root of the transmission of a device consisting of only two grating couplers connected by a short waveguide (length of ≃300 m). Optical coupling to the gratings is achieved using an angled polished fiber-v-groove array equipped with SM fibers for the 900- to 950-nm wavelength range (fiber type: 780HP). The insertion loss of the fiber array (including fiber connector loss and Fresnel loss at the output facet of the array) is calibrated out from the transmission measurement.

Measurement of the modulator insertion loss

The insertion loss of an electrically tunable MZI is estimated by measuring the transmission of the demultiplexer of Fig. 3B for all waveguide inputs. When light is injected into one of the two external inputs, it goes through only one MZI. When light is injected into one of the two internal inputs, it goes through two MZIs. Comparing the total transmission over all outputs between these two cases, we find an average MZI insertion loss equal to 0.8 ± 0.3 dB. This measurement via the demultiplexer structure provides an estimate that is more resilient to variations in the efficiency of other components (e.g., grating couplers and loss in routing waveguides) compared to measuring a single MZI structure (which provided a compatible measurement). We numerically estimate that the insertion loss of our modulators can be lowered to approximately 0.2 dB, at the expense of an increase of ≃2 V in the half-wave voltage, by carefully adjusting the thickness of the cladding and the gap between the electrodes to reduce the amount of metal-induced propagation loss. A further improvement below this value will require an optimization of our fabrication workflow for reducing the effect of sidewall scattering (see Discussion).

For the different circuits reported here, we estimate the per-photon efficiency of the full experimental setup (i.e., including source efficiency, losses in the chip-fiber interfaces, and detection efficiency) to be −30, −24, and −34 for the on-chip single-MZI, de-multiplexer, and 4 × 4 structures, respectively. These values are estimated directly from the detection-per-clock cycle rates. Note that the higher total system efficiency for the on-chip routing experiment is due to the absence of the off-chip demultiplexer for that application (which adds approximately −6 dB loss).

Supplementary Materials

This PDF file includes:
Supplementary Text
Figs. S1 and S2
References

REFERENCES AND NOTES

1. F. Arute, K. Arya, R. Babbush, D. Bacon, J. C. Bardin, R. Barends, R. Biswas, S. Boixo, F. G. S. L. Brandao, D. A. Buell, B. Burkett, Y. Chen, Z. Chen, B. Chiaro, R. Collins, W. Courtney, A. Dunsworth, E. Farhi, B. Foxen, A. Fowler, C. Gidney, M. Giustina, R. Graff, K. Guerin, S. Habegger, M. P. Harrigan, M. J. Hartmann, A. Ho, M. Hoffmann, T. Huang, T. S. Humble, S. V. Isakov, E. Jeffrey, Z. Jiang, D. Kafri, K. Kechedzhi, J. Kelly, P. V. Klimov, S. Knysh, A. Korotkov, F. Kostritsa, D. Landhuis, M. Lindmark, E. Lucero, D. Lyakh, S. Mandrà, J. R. McClean, M. McEwen, A. Megrant, X. Mi, K. Michielsen, M. Mohseni, J. Mutus, O. Naaman, M. Neeley, C. Neill, M. Y. Niu, E. Ostby, A. Petukhov, J. C. Platt, C. Quintana, E. G. Rieffel, P. Roushan, N. C. Rubin, D. Sank, K. J. Satzinger, V. Smelyanskiy, K. J. Sung, M. D. Trevithick, A. Vainsencher, B. Villalonga, T. White, Z. J. Yao, P. Yeh, A. Zalcman, H. Neven, J. M. Martinis, Quantum supremacy using a programmable superconducting processor. *Nature* **574**, 505–510 (2019).

2. Y. Wu, W.-S. Bao, S. Cao, F. Chen, M.-C. Chen, X. Chen, T.-H. Chung, H. Deng, Y. Du, D. Fan, M. Gong, C. Guo, C. Guo, S. Guo, L. Han, L. Hong, H.-L. Huang, Y.-H. Huo, L. Li, N. Li, S. Li, Y. Li, F. Liang, C. Lin, J. Lin, H. Qian, D. Qiao, H. Rong, H. Su, L. Sun, L. Wang, S. Wang, D. Wu, Y. Xu, K. Yan, W. Yang, Y. Yang, Y. Ye, J. Yin, C. Ying, J. Yu, C. Zha, C. Zhang, H. Zhang, K. Zhang, Y. Zhang, H. Zhao, Y. Zhao, Y. Zhou, Q. Zhu, C.-Y. Lu, C.-Z. Peng, X. Zhu, J.-W. Pan, Strong quantum computational advantage using a superconducting quantum processor. *Phys. Rev. Lett.* **127**, 180501 (2021).

3. H.-S. Zhong, H. Wang, Y.-H. Deng, M.-C. Chen, L.-C. Peng, Y.-H. Luo, J. Qin, D. Wu, X. Ding, Y. Hu, P. Hu, X.-Y. Yang, W.-J. Zhang, H. Li, Y. Li, X. Jiang, L. Gan, G. Yang, L. You, Z. Wang, L. Li, N.-L. Liu, C.-Y. Lu, J.-W. Pan, Quantum computational advantage using photons. *Science* **370**, 1460–1463 (2020).

4. L. S. Madsen, F. Laudenbach, M. F. Askarani, F. Rortais, T. Vincent, J. F. F. Bulmer, F. M. Miatto, L. Neuhaus, L. G. Helt, M. J. Collins, A. E. Lita, T. Gerrits, S. W. Nam, V. D. Vaidya, M. Menotti, I. Dhand, Z. Vernon, N. Quesada, J. Lavoie, Quantum computational advantage with a programmable photonic processor. *Nature* **606**, 75–81 (2022).

5. J. Preskill, Quantum computing in the NISQ era and beyond. *Quantum* **2**, 79 (2018).

6. J. Wang, F. Sciarrino, A. Laing, M. G. Thompson, Integrated photonic quantum technologies. *Nat. Photonics* **14**, 273–284 (2020).

7. R. Uppu, L. Midolo, X. Zhou, J. Carolan, P. Lodahl, Quantum-dot-based deterministic photon–Emitter interfaces for scalable photonic quantum technology. *Nat. Nanotechnol.* **16**, 1308–1317 (2021).

8. J. Yin, Y. Cao, Y.-H. Li, S-K. Liao, L. Zhang, J.-G. Ren, W.-Q. Cai, W.-Y. Liu, B. Li, H. Dai, G.-B. Li, Q.-M. Lu, Y.-H. Gong, Y. Xu, S.-L. Li, F.-Z. Li, Y.-Y. Yin, Z.-Q. Jiang, M. Li, J.-J. Jia, G. Ren, D. He, Y.-L. Zhou, X.-X. Zhang, N. Wang, X. Chang, Z.-C. Zhu, N.-L. Liu, Y.-A. Chen, C.-Y. Lu, R. Shu, C.-Z. Peng, J.-Y. Wang, J.-W. Pan, Satellite-based entanglement distribution over 1200 kilometers. *Science* **356**, 1140–1144 (2017).

9. M. Pompili, S. L. N. Hermans, S. Baier, H. K. C. Beukers, P. C. Humphreys, R. N. Schouten, R. F. L. Vermeulen, M. J. Tiggelman, L. dos Santos, B. Martins, S. Dirkse, R. H. Wehner, Realization of a multinode quantum network of remote solidstate qubits. *Science* **372**, 259–264 (2021).

10. D. Llewellyn, Y. Ding, I. I. Faruque, S. Paesani, D. Bacco, R. Santagati, Y.-J. Qian, Y. Li, Y.-F. Xiao, M. Huber, M. Malik, G. F. Sinclair, X. Zhou, K. Rottwitt, J. L. O'Brien, J. G. Rarity, Q. Gong, L. K. Oxenlowe, J. Wang, M. G. Thompson, Chip-to-chip quantum teleportation and multi-photon entanglement in silicon. *Nat. Phys.* **16**, 148–153 (2020).

11. N. C. Harris, G. R. Steinbrecher, M. Prabhu, Y. Lahini, J. Mower, D. Bunandar, C. Chen, F. N. C. Wong, T. Baehr-Jones, M. Hochberg, S. Lloyd, D. Englund, Quantum transport simulations in a programmable nanophotonic processor. *Nat. Photonics* **11**, 447–452 (2017).

12. J. Wang, S. Paesani, Y. Ding, R. Santagati, P. Skrzypczyk, A. Salavrakos, J. Tura, R. Augusiak, L. Man'inska, D. Bacco, D. Bonneau, J. W. Silverstone, Q. Gong, A. Acín, K. Rottwitt, L. K. Oxenløwe, J. L. O'Brien, A. Laing, M. G. Thompson, Multidimensional quantum entanglement with large-scale integrated optics. *Science* **360**, 285–291 (2018).

13. S. Paesani, Y. Ding, R. Santagati, L. Chakhmakhchyan, C. Vigliar, K. Rottwitt, L. K. Oxenløwe, J. Wang, M. G. Thompson, A. Laing, Generation and sampling of quantum states of light in a silicon chip. *Nat. Phys.* **15**, 925–929 (2019).

14. J. M. Arrazola, V. Bergholm, K. Brádler, T. R. Bromley, M. J. Collins, I. Dhand, A. Fumagalli, T. Gerrits, A. Goussev, L. G. Helt, J. Hundal, T. Isacsson, R. B. Israel, J. Izaac, S. Jahangiri, R. Janik, N. Killoran, S. P. Kumar, J. Lavoie, A. E. Lita, D. H. Mahler, M. Menotti, B. Morrison, S. W. Nam, L. Neuhaus, H. Y. Qi, N. Quesada, A. Repingon, K. K. Sabapathy, M. Schuld, D. Su, J. Swinarton, A. Száva, K. Tan, P. Tan, V. D. Vaidya, Z. Vernon, Z. Zabaneh, Y. Zhang, Quantum circuits with many photons on a programmable nanophotonic chip. *Nature* **591**, 54–60 (2021).

15. H. Bombin, I. H. Kim, D. Litinski, N. Nickerson, M. Pant, F. Pastawski, S. Roberts, T. Rudolph, Interleaving: Modular architectures for fault-tolerant photonic quantum computing. arXiv:2103.08612 [quant-ph] (15 March 2021).

16. T. Rudolph, Why I am optimistic about the silicon-photonic route to quantum computing. *APL Photonics* **2**, 030901 (2017).

17. X. Ding, Y. He, Z.-C. Duan, N. Gregersen, M.-C. Chen, S. Unsleber, S. Maier, C. Schneider, M. Kamp, S. Höfling, C.-Y. Lu, J.-W. Pan, On-demand single photons with high extraction efficiency and near-unity indistinguishability from a resonantly driven quantum dot in a micropillar. *Phys. Rev. Lett.* **116**, 020401 (2016).

18. N. Somaschi, V. Giesz, L. De Santis, J. C. Loredo, M. P. Almeida, G. Hornecker, S. L. Portalupi, T. Grange, C. Antón, J. Demory, C. Gómez, I. Sagnes, N. D. Lanzillotti-Kimura, A. Lemaître, A. Auffeves, A. G. White, L. Lanco, P. Senellart, Near-optimal single-photon sources in the solid state. *Nat. Photonics* **10**, 340–345 (2016).

19. R. Uppu, F. T. Pedersen, Y. Wang, C. T. Olesen, C. Papon, X. Zhou, L. Midolo, S. Scholz, A. D. Wieck, A. Ludwig, P. Lodahl, Scalable integrated single-photon source. *Sci. Adv.* **6**, eabc8268 (2020).

20. N. Tomm, A. Javadi, N. O. Antoniadis, D. Najer, M. C. Löbl, A. R. Korsch, R. Schott, S. R. Valentin, A. D. Wieck, A. Ludwig, R. J. Warburton, A bright and fast source of coherent single photons. *Nat. Nanotechnol.* **16**, 399–403 (2021).

21. C. Xiong, X. Zhang, Z. Liu, M. J. Collins, A. Mahendra, L. Helt, M. J. Steel, D.-Y. Choi, C. Chae, P. Leong, B. J. Eggleton, Active temporal multiplexing of indistinguishable heralded single photons. *Nat. Commun.* **7**, 10853 (2016).

22. F. Lenzini, B. Haylock, J. C. Loredo, R. A. Abrahão, N. A. Zakaria, S. Kasture, I. Sagnes, A. Lemaitre, H.-P. Phan, D. V. Dao, P. Senellart, M. P. Almeida, A. G. White, M. Lobino, Active demultiplexing of single photons from a solid-state source. *Laser Photonics Rev.* **11**, 1600297 (2017).

23. F. Kaneda, P. G. Kwiat, High-efficiency single-photon generation via large-scale active time multiplexing. *Sci. Adv.* **5**, eaaw8586 (2019).

24. S. Bartolucci, P. Birchall, H. Bombin, H. Cable, C. Dawson, M. Gimeno-Segovia, E. Johnston, K. Kieling, N. Nickerson, M. Pant, F. Pastawski, T. Rudolph, C. Sparrow, Fusion-based quantum computation. *Nat. Commun.* **14**, 912 (2023).

25. N. C. Harris, Y. Ma, J. Mower, T. Baehr-Jones, D. Englund, M. Hochberg, C. Galland, Efficient, compact and low loss thermo-optic phase shifter in silicon. *Opt. Express* **22**, 10487–10493 (2014).

26. C. Errando-Herranz, A. Takabayashi, P. Edinger, H. Sattari, K. Gylfason, N. Quack, MEMS for photonic integrated circuits. *IEEE J. Sel. Top. Quantum Electron.* **26**, 1–16 (2019).

27. T. Baehr-Jones, R. Ding, Y. Liu, A. Ayazi, T. Pinguet, N. C. Harris, M. Streshinsky, P. Lee, Y. Zhang, A. E.-J. Lim, T.-Y. Liow, S. H.-G. Teo, G.-Q. Lo, M. Hochberg, Ultralow drive voltage silicon traveling-wave modulator. *Opt. Express* **20**, 12014–12020 (2012).

28. M. Dong, G. Clark, A. J. Leenheer, M. Zimmermann, D. Dominguez, A. J. Menssen, D. Heim, G. Gilbert, D. Englund, M. Eichenfield, High-speed programmable photonic circuits in a cryogenically compatible, visible–Near-infrared 200 mm cmos architecture. *Nat. Photonics* **16**, 59–65 (2022).

29. M. Zhang, C. Wang, R. Cheng, A. Shams-Ansari, M. Lončar, Monolithic ultra-high-q lithium niobate microring resonator. *Optica* **4**, 1536–1537 (2017).

30. C. Wang, M. Zhang, B. Stern, M. Lipson, M. Lončar, Nanophotonic lithium niobate electro-optic modulators. *Opt. Express* **26**, 1547–1555 (2018).

31. C. Wang, M. Zhang, X. Chen, M. Bertrand, A. Shams-Ansari, S. Chandrasekhar, P. Winzer, M. Lončar, Integrated lithium niobate electro-optic modulators operating at cmos-compatible voltages. *Nature* **562**, 101–104 (2018).

32. I. Aharonovich, D. Englund, M. Toth, Solid-state single-photon emitters. *Nat. Photonics* **10**, 631–641 (2016).

33. D. White, A. Branny, R. J. Chapman, R. Picard, M. Brotons-Gisbert, A. Boes, A. Peruzzo, C. Bonato, B. D. Gerardot, Atomically-thin quantum dots integrated with lithium niobate photonic chips. *Opt. Mater. Express* **9**, 441–448 (2019).

34. C. Herzog, G. Poberaj, P. Günter, Electro-optic behavior of lithium niobate at cryogenic temperatures. *Opt. Commun.* **281**, 793–796 (2008).

35. F. Thiele, F. Vom Bruch, V. Quiring, R. Ricken, H. Herrmann, C. Eigner, C. Silberhorn, T. J. Bartley, Cryogenic electro-optic polarisation conversion in titanium indiffused lithium niobate waveguides. *Opt. Express* **28**, 28961–28968 (2020).

36. E. Lomonte, M. A. Wolff, F. Beutel, S. Ferrari, C. Schuck, W. H. Pernice, F. Lenzini, Single-photon detection and cryogenic reconfigurability in lithium niobate nanophotonic circuits. *Nat. Commun.* **12**, 6847 (2021).

37. S. Aghaeimeibodi, B. Desiatov, J.-H. Kim, C.-M. Lee, M. A. Buyukkaya, A. Karasahin, C. J. Richardson, R. P. Leavitt, M. Lončar, E. Waks, Integration of quantum dots with lithium niobate photonics. *Appl. Phys. Lett.* **113**, 221102 (2018).

38. I. Christen, M. Sutula, T. Propson, H. Sattari, G. Choong, C. Panuski, A. Melville, J. Mallek, S. Hamilton, P. Dixon, A. J. Menssen, D. Braje, A. H. Ghadimi, D. Englund, An integrated photonic engine for programmable atomic control. arXiv:2208.06732 [quant-ph] (13 August 2022).

39. W. R. Clements, P. C. Humphreys, B. J. Metcalf, W. S. Kolthammer, I. A. Walmsley, Optimal design for universal multiport interferometers. *Optica* **3**, 1460–1465 (2016).

40. J. Lacey, F. Payne, Radiation loss from planar waveguides with random wall imperfections. *IEEE Proc. J. (Optoelectron.)* **137**, 282–289 (1990).

41. E. Lomonte, F. Lenzini, W. H. Pernice, Efficient self-imaging grating couplers on a lithium-niobate-oninsulator platform at near-visible and telecom wavelengths. *Opt. Express* **29**, 20205–20216 (2021).

42. B. Chen, Z. Ruan, X. Fan, Z. Wang, J. Liu, C. Li, K. Chen, L. Liu, Low-loss fiber grating coupler on thin film lithium niobate platform. *APL Photonics* **7**, 076103 (2022).

43. J. J. Renema, A. Menssen, W. R. Clements, G. Triginer, W. S. Kolthammer, I. A. Walmsley, Efficient classical algorithm for boson sampling with partially distinguishable photons. *Phys. Rev. Lett.* **120**, 220502 (2018).

44. J. Rarity, P. Tapster, E. Jakeman, T. Larchuk, R. Campos, M. Teich, B. Saleh, Two-photon interference in a Mach–Zehnder interferometer. *Phys. Rev. Lett.* **65**, 1348–1351 (1990).

45. J. C. Adcock, C. Vigliar, R. Santagati, J. W. Silverstone, M. G. Thompson, Programmable four-photon graph states on a silicon chip. *Nat. Commun.* **10**, 3528 (2019).

46. S. Paesani, M. Borghi, S. Signorini, A. Maïnos, L. Pavesi, A. Laing, Near-ideal spontaneous photon sources in silicon quantum photonics. *Nat. Commun.* **11**, 2505 (2020).

47. A. Kaushalram, G. Hegde, S. Talabattula, Mode hybridization analysis in thin film lithium niobate strip multimode waveguides. *Sci. Rep.* **10**, 16692 (2020).

48. A. L. Migdall, D. Branning, S. Castelletto, Tailoring single-photon and multiphoton probabilities of a single-photon on-demand source. *Phys. Rev. A* **66**, 053805 (2002).

49. M. Varnava, D. E. Browne, T. Rudolph, How good must single photon sources and detectors be for efficient linear optical quantum computation? *Phys. Rev. Lett.* **100**, 060502 (2008).

50. M. Gimeno-Segovia, P. Shadbolt, D. E. Browne, T. Rudolph, From three-photon green-berger-hornezeilinger states to ballistic universal quantum computation. *Phys. Rev. Lett.* **115**, 020502 (2015).

51. H. Wang, J. Qin, X. Ding, M.-C. Chen, S. Chen, X. You, Y.-M. He, X. Jiang, L. You, Z. Wang, C. Schneider, J. J. Renema, S. Höfling, C.-Y. Lu, J.-W. Pan, Boson sampling with 20 input photons and a 60-mode interferometer in a 10^{14}-Dimensional hilbert space. *Phys. Rev. Lett.* **123**, 250503 (2019).

52. J. Carolan, C. Harrold, C. Sparrow, E. Martín-López, N. J. Russell, J. W. Silverstone, P. J. Shadbolt, N. Matsuda, M. Oguma, M. Itoh, G. D. Marshall, M. G. Thompson, J. C. F. Matthews, T. Hashimoto, J. L. O'Brien, A. Laing, Universal linear optics. *Science* **349**, 711–716 (2015).

53. J. Huh, G. G. Guerreschi, B. Peropadre, J. Mcclean, A. Aspuru-Guzik, Boson sampling for molecular vibronic spectra. *Nat. Photonics* **9**, 615–620 (2015).

54. C. Sparrow, E. Martín-López, N. Maraviglia, A. Neville, C. Harrold, J. Carolan, Y. N. Joglekar, T. Hashimoto, N. Matsuda, J. L. O'Brien, D. P. Tew, A. Laing, Simulating the vibrational quantum dynamics of molecules using photonics. *Nature* **557**, 660–667 (2018).

55. E. Lomonte, M. Stappers, F. Lenzini, W. Pernice, Highly efficient silicon nitride grating couplers with metal back-reflector enabled by cryogenic deep silicon etching, in *Integrated Photonics Platforms II* (SPIE, 2022), vol. 12148, pp. 14–18.

56. N. Lindenmann, G. Balthasar, D. Hillerkuss, R. Schmogrow, M. Jordan, J. Leuthold, W. Freude, C. Koos, Photonic wire bonding: A novel concept for chip-scale interconnects. *Opt. Express* **20**, 17667–17677 (2012).

57. J. Borregaard, H. Pichler, T. Schröder, M. D. Lukin, P. Lodahl, A. S. Sørensen, One-way quantum repeater based on near-deterministic photon-emitter interfaces. *Phys. Rev. X* **10**, 021071 (2020).

58. F. T. Pedersen, Y. Wang, C. T. Olesen, S. Scholz, A. D. Wieck, A. Ludwig, M. C. Löbl, R. J. Warburton, L. Midolo, R. Uppu, P. Lodahl, Near transform-limited quantum dot linewidths in a broadband photonic crystal waveguide. *ACS Photon.* **7**, 2343–2349 (2020).

59. Y. Wang, C. F. Faurby, F. Ruf, P. I. Sund, K. H. Nielsen, N. Volet, M. J. Heck, N. Bart, A. D. Wieck, A. Ludwig, L. Midolo, S. Paesani, P. Lodahl, Deterministic photon source interfaced with a programmable silicon-nitride integrated circuit. arXiv:2302.06282 [quant-ph] (13 February 2023).

60. J. P. Salvestrini, L. Guilbert, M. Fontana, M. Abarkan, S. Gille, Analysis and control of the DC drift in LiNbo3based Mach–Zehnder modulators. *J. Light. Technol.* **29**, 1522–1534 (2011).

61. J. F. F. Bulmer, S. Paesani, R. S. Chadwick, N. Quesada, Threshold detection statistics of bosonic states. *Phys. Rev. A* **106**, 043712 (2022).

62. S. Scheel, Permanents in linear optical networks. arXiv:quant-ph/0406127v1 (2004). https://doi.org/10.48550/arXiv.quant-ph/0406127.

63. S. Aaronson, A. Arkhipov, The computational complexity of linear optics, in *Proceedings of the Forty-Third Annual ACM Symposium on Theory of Computing* (ACM, 2011), pp. 333–342.

Science Advances

High-speed thin-film lithium niobate quantum processor driven by a solid-state quantum emitter

Patrik I. Sund, Emma Lomonte, Stefano Paesani, Ying Wang, Jacques Carolan, Nikolai Bart, Andreas D. Wieck, Arne Ludwig, Leonardo Midolo, Wolfram H.P. Pernice, Peter Lodahl, and Francesco Lenzini

View the article online
https://www.science.org/doi/10.1126/sciadv.adg7268
Permissions
https://www.science.org/help/reprints-and-permissions

Use of this article is subject to the Terms of service